Supplementary Materials for

Nuclear Pore Scaffold Structure Analyzed by Super-Resolution Microscopy and Particle Averaging

Anna Szymborska, Alex de Marco, Nathalie Daigle, Volker C. Cordes, John A. G. Briggs, Jan Ellenberg*

*Corresponding author. E-mail: jan.ellenberg@embl.de

This PDF file includes:

Materials and Methods
Supplementary Text
Figs. S1 to S9
Tables S1 to S3
References

Materials and Methods

<u>Antibodies</u>

The primary antibodies used in this study are listed in Table S1. Detection was achieved with goat anti-rabbit, anti-guinea pig or anti-mouse IgG highly cross-absorbed secondary antibodies coupled to Alexa Fluor 647 (for super-resolution (SR) microscopy), Alexa Fluor 532 (for second channel in double-color SR microscopy) or Alexa Fluor 488 or Alexa Fluor 546 (for confocal microscopy; all from Life Technologies). The (m)EGFP tagged Nups were detected using an anti-GFP nanobody (GFP-trap, Chromotek) (21), conjugated to Alexa Fluor 647 using NHS-ester chemistry (Life Technologies).

<u>Constructs</u>

Full–length cDNA of nucleoporins used in this study were tagged at N- or C-terminus with either EGFP or mEGFP (29). Nup coding sequences fused to mEGFP were cloned into the backbone of pEGFP-N1. Mammalian expression was driven by the human cytomegalovirus immediate early promoter. Each construct was made siRNA-resistant by introducing 3 or 4 silent mutations. For the details on the generated constructs see Table S2.

<u>RNAi</u> <u>knock-down</u>

SiRNA knock-down of selected Nups was carried out using pre-designed Silencer Select siRNAs (Life Technologies, for details see Table S3). The cells were transfected with siRNAs by solid phase transfection on siRNA-coated 24-well plates. The plates were coated using a modified protocol from Erfle et al. (30). In brief, transfection mix was prepared by combining 0.4 M sucrose/Opti-MEM (Life Technologies), Lipofectamine 2000 (Life Technologies) diluted 1:2 in ddH2O and 3μM siRNA at 1.7:1:2.8 ratio and incubated for 20 min at room temperature. The reagents were then gently mixed with 0.2% gelatine at 1:0.6 ratio. The transfection mix was then diluted at 1:50 in ddH2O and distributed into wells of a 24-well plate using 1.6 pmols of siRNA per well. The plates were immediately dried in miVac vacuum concentrator (GeneVac, Ltd) at 37°C and stored in sealed boxes with drying pearls for further use.

<u>Cell</u> <u>culture</u> <u>and</u> <u>sample</u> <u>preparation</u>

Human osteosarcoma U2OS cells were cultured in DMEM supplemented with 10% fetal bovine serum, according to standard protocols. Immunofluorescence was performed using an adapted protocol from Krull et al. (31). Briefly, the cells were grown overnight on 8-well Lab-Tek Chambered Coverglass (Thermo Fisher Scientific). The cells were then rinsed with 2.4% PFA (Electron Microscopy Sciences) in PBS and extracted with 0.4% Triton X-100 (Sigma Aldrich) in PBS for 3 min. Next, the cells were fixed for 30 min with 2.4% PFA in PBS, quenched for 5 min with 50 mM NH$_4$Cl, then extensively washed with PBS, and blocked with 5% normal goat serum (Life Technologies) in PBS (blocking buffer) for 1 hour. Subsequently, the cells were incubated overnight at 4°C with primary antibodies freshly diluted in the blocking buffer, and then with secondary antibodies for 1 hour at room temperature.

For experiments with GFP-tagged nucleoporins, U2OS cells were transected with the appropriate construct using Fugene 6 (Promega). 24 hours later the cells were

transferred onto 24-well plate coated with a matching siRNA. After another 48 hours, the cells were split onto gridded cover slips (50μm grid spacing, IBIDI), which facilitated identification of cells with the appropriate expression levels of Nup-GFP. For imaging we were selecting cells with high level of incorporation of the tagged Nup into the pore, characterized by brightness and low cytoplasmic and nucleoplasmic background, which did not exhibit pore clustering or aberrant nuclear shape phenotypes indicative of large over-expression of Nups. 16 hours later, the cells were extracted and fixed as described above. Next, the samples were incubated for 30 min with a few drops of Image-iT FX Signal Enhancer solution (Life Technologies) and then blocked for 1 hour with 5% BSA in PBS. Finally the samples were incubated with Alexa Fluor 647-conjugated anti-GFP nanobody diluted in 5% BSA/PBS for 90 min and then washed 3 times for 5 min with PBS.

Differential permeabilization of the cells was achieved by 4 min incubation on ice with 33 μg/ml Digitonin in a buffer containing 20 mM HEPES pH 7.3, 110mM CH_3COOK, 5mM CH_3COONa, 2 mM $Mg(CH_3COO)_2$ and 1mM EGTA, prior to fixation. The samples were then fixed and blocked as described above and stained with anti-GFP nanobody and 133A2-LaminA, detected with Alexa Fluor 546 conjugated secondary antibody.

All samples were imaged immediately after preparation.

Confocal microscopy

Single confocal sections (FWHM 0.8 µm) of cell nuclei were acquired on a Zeiss LSM 780 microscope, using alpha Plan-Apochromat 100x, NA 1.46 objective, with xy pixel size set to 0.042 µm. Samples were imaged in PBS.

Super-resolution imaging

All SR imaging was performed on a Leica SR GSD microscope, equipped with a 500 mW 642 nm and 1000 mW 532 nm continuous wave lasers (MPBC, Inc.); a 30 mW 405 nm diode laser (Coherent, Inc.); a DBP 405/10 642/10 excitation filter; an MBP 405/488/561/635 excitation filter (used in double color experiments); an LP 649 and LP 541 dichroic mirror; a BP 710/100 and BP 600/100 suppression filters; Leica HCX PL APO 100x, NA 1.47 Oil CORR TIRF PIFOC objective; and an additional 1.6x magnification lens. The image was collected on an Andor iXon3 897 EMCCD camera, with a final optical pixel size of 100 nm. The lateral drift was minimized by the Suppressed Motion (SuMo) stage.

The samples were embedded in GLOX-MEA imaging buffer (32), containing: glucose oxidase-based oxygen scavenging system (GLOX, 0.5 mg/ml glucose oxidase, 40 µg/ml catalase, 10% w/v glucose); 50 mM Tris-HCl, pH 8.0; 10 mM NaCl; and 10 mM β-Mercaptoethylamine (MEA, prepared from solid at 100 mM in PBS and adjusted with HCl to pH 7.4, stored at -20°C). The buffer was prepared fresh and exchanged after approximately 90 minutes of imaging.

In order to bring the fluorophores into dark states, the sample was first illuminated with 642 nm light at the maximum laser power, until single fluorophore blinking behavior was observed, typically for less than 30 s. Next, a long series was acquired at intermediate laser power, at a rate of 100 frames per second. To determine the minimal length of the series, which generates SR images of sufficient quality for single particle

averaging, we reconstructed images of Nup133-FL-labled cells using a decreasing number of frames. We then averaged particles from these images and measured the average radial position of the Nup133-FL label (see: "Iterative translational alignment" and "Estimation of radial position and cross-validation analysis") and found that the measurement became stable above 20,000-40,000 frames. We therefore used only series with at least 40,000 frames for SR image reconstruction (Fig. S2A).

In order to facilitate the return of fluorophores to the ground state at a constant rate, the sample was illuminated with the 405 nm back-pumping laser; the gradual increase of the 405 nm laser intensity was achieved either manually or by the GSD Wizard's "Auto Backpumping" feature. Imaging was performed in epifluorescence mode.

For double color imaging, the cells were plated on Lab-Tek coverglass coated with 100 nm Tetraspeck microspheres (Life Technologies) which served as registration marks for the alignment of the two channels. We acquired the single fluorophore blinking series sequentially, starting with the 642 nm channel and then registered the datasets as described before (32). Our final registration error across the whole field of view was ~ 7 nm.

<u>Single fluorophore localization, drift correction and image reconstruction</u>

All image processing and computer simulations in this study, unless otherwise stated, were performed in Matlab 2010®, (The Mathworks, Inc).

Single fluorophore blinking events were localized with a fast centroid fit, implemented in the Leica SR GSD Wizard, using 25 photons per pixel as the detection threshold. The integrated intensity of an individual event was calculated as the number of photons collected after background subtraction, divided by the camera calibration factor determined by the manufacturer. To exclude events with low localization precision, those with an integrated intensity of less than 500 photons were filtered out.

The lateral drift in the images was corrected using an adapted correlation-based method (32, 33). Briefly, the localization data was split into equal segments of several thousand frames and an SR image was reconstructed from each segment. A correlation map between adjacent segments was calculated using the Kuglin-Hines algorithm (34). The position of the peak in the correlation map was determined by a 2D Gaussian fit and the relative shift was calculated as a difference between peak positions in subsequent maps. The final drift curves were generated by linear interpolation and then subtracted from the localization data. The procedure was iterated until no residual drift was observed.

The final SR images were reconstructed from the intensity-filtered and drift-corrected sets of localizations using 10 nm pixelation. Each localization event was rendered as a single gray value of a 16-bit image.

<u>Evaluation of localization precision</u>

The resolution in SR images depends, among other parameters, on how precisely a single fluorescently labeled marker can be localized. To estimate this we utilized spatially isolated clusters of localizations, which originate with a high probability from single antibodies. Isolated localizations appeared in our images as clusters of single fluorophore events that occurred between nuclear pores (Fig. S1B).

To estimate the overall localization precision in each image, 25-35 isolated clusters were cropped manually in 300x300 nm boxes, and any extraneous signal was masked. Each cluster was then fitted with a 2D Gaussian and the overall localization precision was calculated as the average full-width at half maximum (FWHM) of the peaks. If the average localization precision of an image was worse than 30 nm, it was not considered for further analysis.

Selection and quality control of the particles

Individual pores were interactively cropped as single particles from SR images in 300x300 nm boxes using Boxer (EMAN1 image processing package, BCM), excluding those at the edge of the nucleus. The particles were then controlled for high quality and completeness of labeling prior to accepting them for averaging.

Pre-alignment and masking of background: First, images of all cropped particles from one experiment were translationally aligned in three iterations (see: "Iterative translational alignment"), then summed and rotationally averaged. The rotational average was then Otsu thresholded and dilated to create a binary mask, which excluded background signal outside the pore structure (Fig. S1C, left panel).

Number of events per particle: In order to determine the number of single fluorophore blinking events associated with each particle, signal inside the mask in the raw aligned images was summed.

Number of localization clusters per particle: The aligned images of particles were masked and transformed to a polar coordinate system [r, φ], by measuring the linear intensity profile from the center of the average image towards the edge every 6°. The signal was then summed along the r axis (Fig. S1C, upper right panel) and decomposed into a minimal number of Gaussians of different amplitude (determined by the number of single fluorophore blinking events per peak) but with the same width (determined by the localization precision of the SR image adjusted for low pass filtering and polar transformation) (Fig. S1C, lower right panel). Fitting was performed using PeakFinder (35).

Iterative translational alignment

A set of particles was summed and rotationally averaged to generate an initial reference. Individual pores were then translationally aligned using sub-pixel shifts calculated based on the center of mass of a correlation peak between the images of the pore and the reference. The translated images were then summed and rotationally averaged to generate the subsequent reference. This procedure was iterated until no further change in the measured radial distance was observed, typically seven times. Images were normalized and low-pass filtered to 28 nm in order to reduce the noise. The final average image was then generated by summing of all quality controlled particles translationally aligned to the final reference (Fig. 1D). The processing was done using IMAGIC (Image Science Software, GmBH).

Estimation of the average radial position and cross-validation analysis

In order to characterize the localization clusters, which originated from single antibodies and formed the ring-shaped particles, we stained the cells using limiting amounts of the primary antibody to obtain only partial decoration of the NPC. In the SR

images of these samples, individual subunits of the pores appeared as 2D Gaussian-shaped clusters, with a spread equal to the localization precision of the image. The individual ring structures we observed are therefore composed of small Gaussians arranged in a circle around the center of the pore (Fig. S3).

The average image of the particle is therefore generated by summing many such localization clusters in the shape of 2D Gaussian peaks, arranged in a circle with the radius R. To estimate the real radius R, the convolution of 2D Gaussians with a circle, which results in a characteristic "doughnut" shape and an apparent shift of the maximum of the intensity profile towards the center of the particle, have to be taken into account. Such shape can be described with the following equation, referred to here as a circularly convolved Gaussian:

$$f(x, y) = A \cdot \int_0^{2\pi} e^{-\frac{(x - R\cos\varphi)^2 + (y - R\sin\varphi)^2}{2\sigma^2}} d\varphi = 2\pi \cdot A \cdot e^{-\frac{x^2 + y^2 + R^2}{2\sigma^2}} \cdot I_0(\frac{R}{\sigma^2}\sqrt{x^2 + y^2})$$

Eq. 1

where: x, y –coordinates in the average image; R – radial position of the localization clusters; φ – angular position of the 2D Gaussian peak; σ, A – spread and amplitude of the 2D Gaussian peak, I_0 – modified Bessel function of the first kind.

For a linear profile in any direction $x^2 + y^2 = r^2$, therefore:

$$f(r) = 2\pi \cdot A \cdot e^{-\frac{r^2 + R^2}{2\sigma^2}} \cdot I_0(\frac{R}{\sigma^2} \cdot r)$$

Eq. 2

To determine the mean radial position R of the clusters, the average image of the particle was transferred into a polar coordinate system [r, φ] and the mean intensity along the φ direction was calculated. This linear profile was then normalized between 0 and 1 and fitted with Eq. 2 using a least squares method in the Matlab Curve Fitting toolbox, with starting parameters estimated from an initial spline fit of the profile (Fig. 1E). Radius R was determined from the multi-parameter fit.

In order to estimate the precision with which we can measure R, we performed cross-validation analysis on the Nup133 data (Fig. 1F). All pores that passed quality control were pooled into one dataset of 8,698 pores. The data was then split into random, non-overlapping subsets of 500 pores, averaging was performed on each subset and precision of the measurement was calculated as the standard deviation of the average radial positions from the subsets.

To ensure that inter-experimental variation between stainings is taken into account, the mean radial positions of all markers used in this study were determined by separately averaging pores from each independent staining experiment performed with the respective marker. The error was calculated as the standard error of the mean of the experiments, and the 95% confidence interval for the position of the label as R ± 1.96 · SEM. The significance level of the differences between the positions of respective markers was determined using pairwise t-tests, with p-values corrected for multiple testing with Benjamini and Hochberg method (36). Statistical analysis was performed using R (R Foundation for Statistical Computing, Vienna, Austria).

Simulations

To further validate our method and determine the minimal quality criteria of the particles, which ensure reliable averaging, we performed a series of computer simulations of particles with controlled properties.

The in silico generated particles were composed of several localization clusters, each placed in one of eight positions equidistantly distributed in a circle of radius R representing the eightfold symmetry of the pore complex. Each cluster was rendered as a 2D Gaussian peak with a FWHM = 30 nm. The particles were then rotated by a random angle, translated off-center and scaled to a 10 nm pixel size to mimic our experimental data. Next, the particles were passed through the averaging procedure we used for our experimental data.

As described above (see: "Selection and quality control of particles"), we first varied the number of the localization clusters per particle and evaluated how accurately we can determine the original radial position of the clusters by our averaging and fitting procedure (Fig. S2C).

Next, we wanted to know how accurately we can measure R in particles with similar properties to those we observed experimentally (Fig. S4). To do that, we generated a dataset in which each particle was formed by clusters whose number was pulled from a normal distribution with the same mean ($\mu = 7$) and standard deviation ($\sigma = 0.5$) as observed in Nup133-FL-labeled pores. Furthermore, our experimental structures were not always perfectly circular, presumably because antibodies do not always bind to their epitopes from the same direction. In the second set of data we allowed the position of the localization clusters to randomly deviate from R in any direction by a small distance d pulled from a normal distribution. The center of the localization cluster varied from R in the range of 0 to 15 nm – the approximate length of the primary and secondary antibody (37).

For each case, we generated 20 sets of 500 particles with radius R = 50 nm, averaged each set individually and found that we can measure the mean radius with subnanometer accuracy even if the shape of the particles deviates from the perfect circle due to random orientation of antibody binding (Fig. S4).

Particle alignment on a molecular reference

The single particle averaging concepts presented here should in principle be applicable to other large protein complexes. However, the translational alignment method we used relies on the intrinsic symmetry of the complex. Therefore we wanted to test if particles can be precisely aligned using a molecular reference labeled in a second color. To this end we stained U2OS cells with pairs of antibodies: Nup133-aa566-582 detected with secondary antibody coupled to Alexa Fluor 647 and Nup62-aa24-178 (Alexa Fluor 532); Seh1-FL (Alexa Fluor 647) and Nup62-aa24-178 (Alexa Fluor 532). We then acquired four to six double color images per pair of antibodies (Fig. S8 A, C). Next, we manually picked 100-200 double-color particles from each image.

We then aligned the particles in the 532 nm channel, using the procedure described in "Iterative translational alignment" and applied the calculated shifts to the respective images in 642 nm channel. We calculated the average images by summing all aligned particles from each channel (Fig. S8B, D: left panels). We determined the normalized average intensity profile as described in "Estimation of radial position", this time using

the center of 532 nm signal as the starting point. We then fitted the average intensity profiles with Eq. 2 (Fig. S8 B, D: right panels). To estimate the precision of this alignment we performed a crossvalidation analysis by splitting each dataset into several non-overlapping subsets of 150 pores each, and performing the alignment and fitting within each subset independently.

<u>Triangulation of relative protein positions in asymmetric complexes</u>
To further demonstrate the potential of SR-based methods for defining the relative positions of proteins in asymmetric complexes, we generated an artificial dataset from the images described in section "Particle alignment on a molecular reference". Briefly, the dataset consisted of double-color images of the following pairs of antibody stainings: Nup133 (Alexa Fluor 647) and Nup62 (Alexa Fluor 532); Seh1 (Alexa Fluor 647) and Nup62 (Alexa Fluor 532); and Nup133 (Alexa Fluor 647) and Seh1 (Alexa Fluor 532). From these images we manually selected 642 nm-532 nm pairs of localizations clusters (Fig. S9, A, C, E). A pair of clusters was selected if (i) it was sufficiently far from other localizations to contain only one peak in each channel and (ii) the 642 nm cluster was close enough to a cluster in the 532 nm channel to assume that both come from the same pore (for Nup62 pairs) or the same "spoke" (Nup133-Seh1). The position of each cluster was determined by calculating the center of all localization events it contained. We then calculated the Euclidean distance l between the 642 nm - 532 nm cluster pairs (Fig. S9 B, D, F). As discussed extensively in Churchman et al. (38), such measurement generates a non-Gaussian distribution. In order to determine the mean distance between the markers, we performed a maximum likelihood fit (Matlab Statistics Toolbox) of the distributions to a function:

$$p_{2D}(l) = (\frac{l}{\sigma^2})\exp(-\frac{\mu^2 + l^2}{2\sigma^2})I_0(l\mu/\sigma^2)$$

Eq. 3

where: l - distance between marker positions; σ^2 – variance of l; μ – mean distance between 2 markers; I_0 - modified Bessel function of the first kind.
Knowing the mean distances μ between each pair of markers we calculated the relative positions of all three proteins using elementary geometry (Fig. S9G).
In this simplified proof-of-principle case we still took advantage of the fact that all of the particles in the dataset were arranged similarly along the optical axis. However, this concept can be easily extended to third dimension if combined with 3D super-resolution imaging, removing the requirement for preferential arrangement of the complexes.

Supplementary Text
<u>Overview of the quality control pipeline</u>
In order to ensure reproducibility and comparability of the radius measurement between different molecular labels and nucleoporins, we applied quality control at every data analysis step, employing thresholds validated experimentally, using the Nup133-FL

datasets, or by computer simulations (Figs. S1-2). In brief, in the resulting automated and unbiased method, we used only images reconstructed from bright blinking events (Fig. S1A), rejected images with low localization precision (Fig. S1B) and accepted only ring-like structures with high labeling density for averaging (Figs. S1C, S2. C-D).

To establish a minimal number of events per particle, which allows for stable alignment, we reconstructed images of decreasing quality by randomly removing events from seven localization datasets of Nup133-FL-labled cells (Fig S2B). The averaging procedure in the examined SR datasets started yielding a stable measurement when the particles contained at least 250 events on average. We chose a conservative threshold of 500 localized events for particles labeled with antibodies to be retained for further analysis. This threshold needed to be adjusted to the number of dyes on the labeling reagent. Since one nanobody was conjugated to 1 dye on average, approximately 5x less than the secondary antibody, we lowered this threshold to 100 events for particles labeled with the nanobody.

In order to determine the minimal number of clusters per particle, which allows for stable alignment, we simulated particles (see: "Simulations") with three different radii, varying the number of localization clusters (Fig. S2C). Particles containing less than five clusters yielded a measurement with an unacceptably high error; therefore in our experimental data, only particles with at least five detectable clusters were retained for further analysis.

Finally, we determined the minimal number of particles necessary for stable measurement of the radial position. To do that we took quality-controlled particles from four independent Nup133-FL stainings and randomly sorted them into subsets containing an increasing number of particles. We performed averaging in each subset individually and observed that ~500 particles are sufficient for obtaining a stable measurement (Fig. S2D). We therefore only used experiments, which yielded 500 or more high quality particles.

Additional controls

In this study we measured the average positions of the endogenous Nup107-160 components using antibodies raised against small fragments of the respective nucleoporins (Fig. 2). In order to control for effects of individual antibodies, we mapped the most extremely positioned Nups with independent antibodies raised against the full-length proteins, Nup133-FL and Seh1-FL (Fig. S6). The results we obtained were very similar with the difference of only 0.6 nm, for Seh1 and 1.5 nm, for Nup133.
To exclude the possibility that the peripheral position of the Nup160 arm was due to the immuno-reagent binding from the nuclear envelope lumen, we estimated the positions of Nup160-C and Nup160-N GFP fusions in differentially permeabilized cells where access was only possible from the cytoplasm (Fig. S7). The approximate mean radial positions of these two markers were 41 nm (C-term) and 55 nm (N-term), qualitatively confirming the result obtained from the Triton permeabilized cells (Fig. 3). This indicates that the nanobody in our standard measurements reaches the Nup160 fusion proteins from the cytoplasmic and nucleoplasmic sides, rather than from the NE lumen. The slight difference between the measurements is likely due to the presence of intact membranes in the differentially permeabilized samples or due to subtle effects of the detergent on the morphology of the pore.
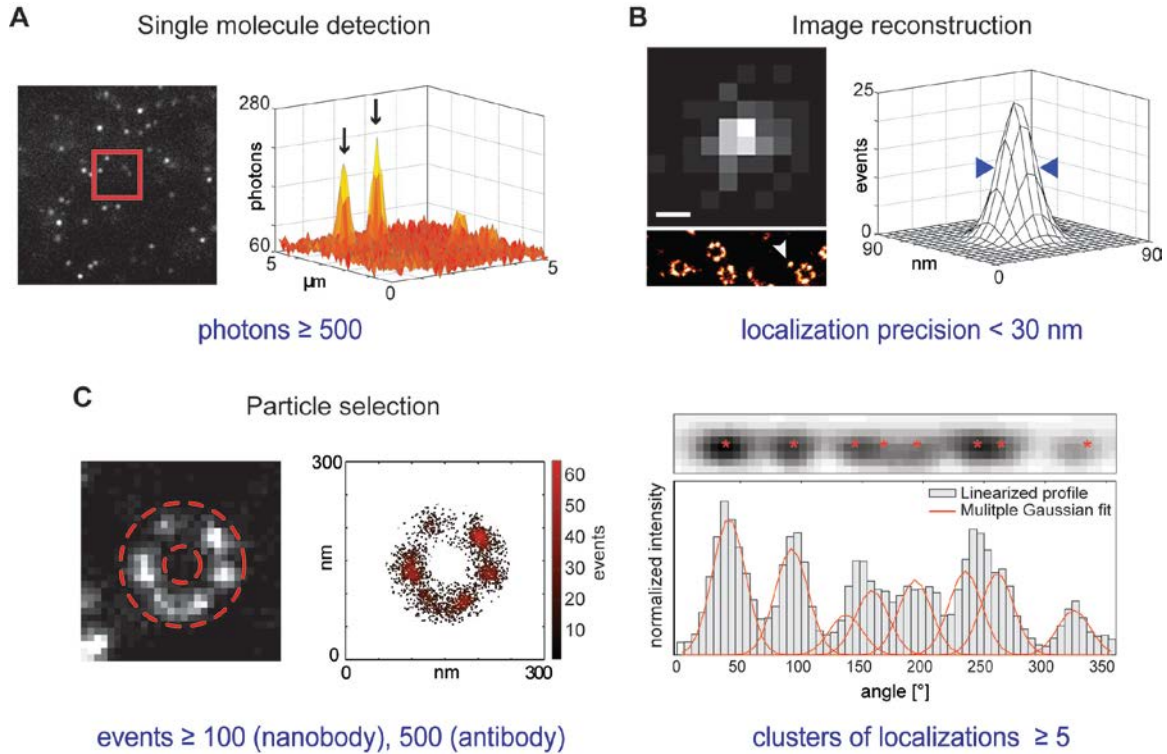
A Single molecule detection

photons ≥ 500

B Image reconstruction

localization precision < 30 nm

C Particle selection

events ≥ 100 (nanobody), 500 (antibody)

clusters of localizations ≥ 5

Fig. S1. Quality control of the SR data for particle averaging.

(**A**) A 10 ms frame from a localization microscopy time series (left). The photon counts detected in a 5 µm^2 area (red box), plotted on the right, illustrate two typical single fluorophore blinking events (arrows) with an integrated intensity over background larger than 500 photons, the threshold used for image reconstruction. (**B**) Total signal from all blinking events produced by a single antibody bound between the NPCs (upper left), visible as a spatially isolated cluster of localizations indicated with an arrowhead (lower left). Scale bar: 20nm. The localization precision for this antibody corresponds to the full width at half maximum of a fitted 2D Gaussian (blue arrows, right). We required the overall localization precision in the image to be below 30 nm. (**C**) An image of a typical particle in a 300 x 300 nm box (left) and a density plot of single fluorophore blinking events (central). We quantified the number of events associated with the pore using an automatically generated mask (red dashed circles) and imposed a threshold of 500 events for antibody-stained pores and 100 events for nanobody-stained pores to pass further in the analysis. Right panels: An image and a histogram of the linearized circular intensity profile of the particle with eight clusters of localizations (red asterisks), automatically detected by fitting the histogram (gray bars) with the minimal number of fixed-width Gaussians (red line). We required at least 5 clusters of localizations detectable around the particle's center to ensure a stable translational alignment.
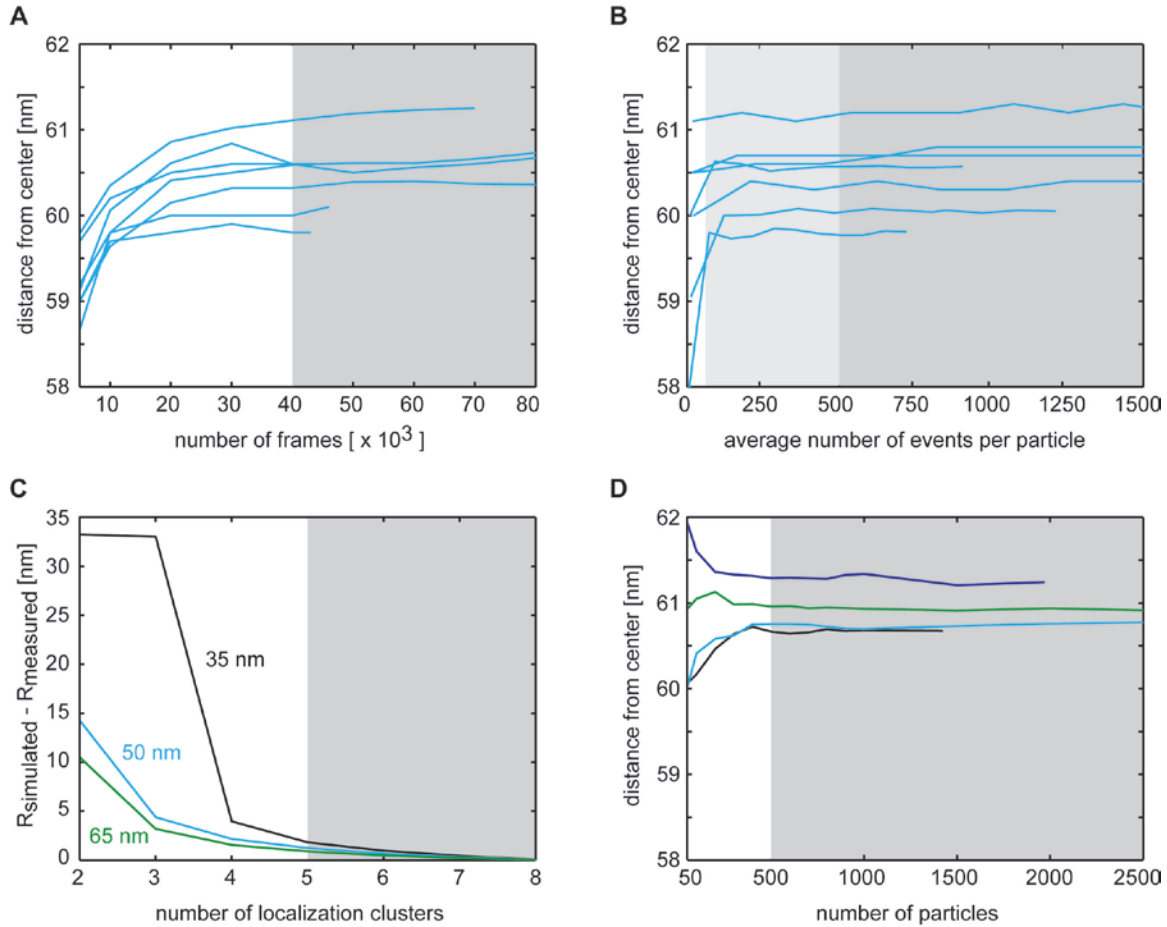
Fig. S2. Determination of the thresholds for the quality control of the data.
(A) Dependence of the stability of the radius measurement on the number of frames used for reconstruction of the SR image. Images of seven Nup133-FL-stained cells were reconstructed using the first 10,000; 20,000; 30,000 etc. frames of the single molecule blinking sequence. For each dataset, the same particles were cropped (400-600 per image) and averaged. The measured radial distance was plotted against the number of frames used. The measurement becomes stable above 20,000-40,000 frames, the gray area indicates the conservative threshold of at least 40,000 frames used in this study. **(B)** Dependence of the stability of the radius measurement on the average number of single fluorophore blinking events per particle. Images from (A) were reconstructed from localization datasets reduced by removing an increasing number of randomly chosen events, in order to simulate decreasing signal over background. For each dataset, the same particles were cropped and averaged. The measured radial distance was plotted against the average number of events per pore. The gray area indicates the threshold of 500 events (darker gray) used in this study for the analysis of antibody stained pores and 100 events used for the nanobody-stained pores (light gray) **(C)** Dependence of the accuracy of the radius measurement on the completeness of labeling of the pore. We generated sets of 1,000 particles in silico with R=35 nm (black), 50 nm (blue) or 65 nm (green), formed by two to eight localization clusters, and averaged particles in each set separately. We plotted the difference between the simulated and the measured radial

positions against the number of clusters. If the pores are poorly decorated by the antibodies, the radial positions of the labels are always underestimated, due to imprecise alignment. We therefore imposed a threshold of at least five detectable clusters on our experimental data, as indicated by the gray shading. **(D)** Dependence of the stability of the radius measurement on the number of particles. Particles from four independent Nup133-FL stainings were sorted into subsets containing from 50 to 2,500 particles. The measured radial distance for each subset was plotted against the number of particles in that subset. The measurement is stable above 400 particles, the gray area indicates the conservative threshold of 500 particles used in this study.
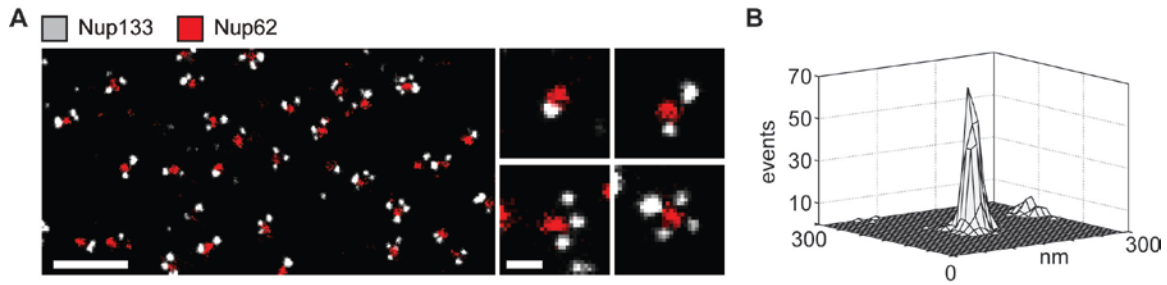
Fig. S3. Images of nuclear pores are composed of several 2D-Gaussian shaped clusters.

(A) Left panel: A representative 4.5 μm^2 area of the lower surface of the nucleus of a U2OS cell stained with a limiting amount of primary antibody Nup133-FL (grayscale signal), co-immuno-labeled with an antibody Nup62-aa24-178 (red signal) to mark the center of each pore. Right panels: Individual particles with 1, 2, 3 or 4 localization clusters. Scale bars: 0.5 μm and 0.1 μm from left to right. **(B)** The Nup133 localization cluster shown in top central panel, presented as a surface plot. The shape is a 2D Gaussian peak, with a spread equal to the localization precision of the SR image. A fully labeled particle is composed of several such clusters arranged in a circle.
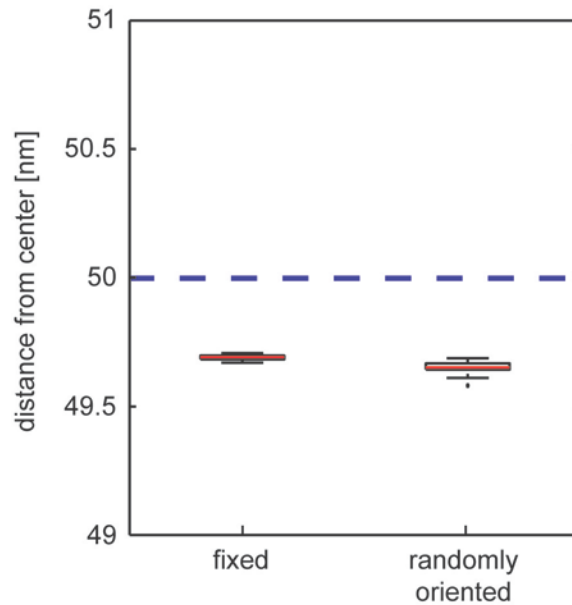
Fig. S4. The radial position of the fluorescence marker can be determined to subnanometer accuracy.

Particles with radius R = 50 nm and a number of subunits mimicking the experimental data for Nup133-FL were generated in silico. The localization clusters were placed either in fixed positions on the circle ("fixed") or allowed to deviate by a maximum 15 nm in any direction to mimic a random orientation of the antibody pair ("randomly oriented"). The boxplot shows the results of averaging of 20 sets of 500 particles each. Assuming that the antibody pair binds directly above the epitope along the optical axis or orients randomly about the epitope, the measured position of the fluorophore is equivalent to the position of the epitope and can be determined with 0.35 nm accuracy and 0.1 nm precision. Since the exact spatial relationship between the antibody pair and the epitope is not known, the position of the epitope might be systematically under- or overestimated if the antibody binds at a preferred angle. However, immunolabeling is currently the only method which allows for comparison between several endogenous Nups.
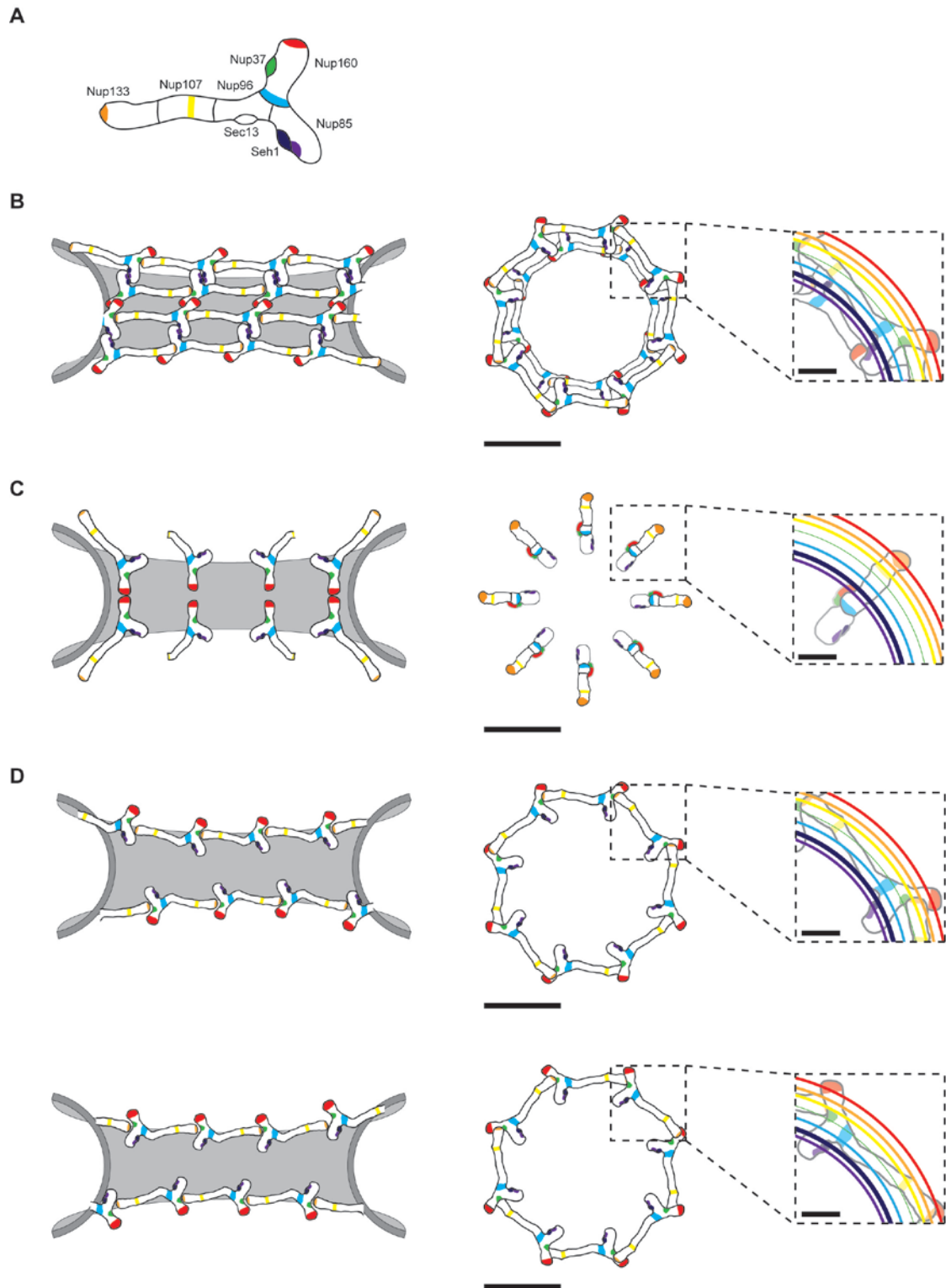
**Fig. S5. Different models for the organization of the NPC scaffold.**

Comparison of different models for the organization of the NPC scaffold, schematically represented in side-view (left panels) and top-view (central panels). The different

domains of the Y-shaped complex are color coded as in Fig. 3 and Fig. 4 to show the positions of the Nups mapped using (m)EGFP-nanobody labeling. The right panels show a close-up on a fragment of the pore, with the measured average radial positions overlaid as rings on top of the model as in Fig. 4. Scale bars are 40 nm and 10 nm from left to right. **(A)** Schematic representation of the color-coded Y-shape complex from Fig. 3 for reference. **(B)** "Fence-like coat" model, proposed for the first time by Hsia et al. (19, 25), based primarily on the crystal packing of yNup85-ySeh1 and yNup145C-ySec13. In this model, eight Y-shaped complexes are arranged circumferentially in a head-to-tail fashion via yNup120-yNup133 interaction. Four octameric rings are stacked in anti-parallel orientation, and span the full height of the NPC coat. The four rings are connected by vertical poles formed by hetero-octamers of either yNup85-ySeh1 or yNup145C-ySec13. In the top-view, such arrangement would predict two zones of localization or a broad distribution of the Nup160 and Nup133 signal, resulting from the anti-parallel stacking of the four rings. Additionally, this model predicts that the signal of all six Nups should overlap with the EM density of the spoke-ring, contrary to our observations. Therefore our data is inconsistent with this model. **(C)** "Lattice" model (18, 26), based on the structural homology of the scaffold Nups and the proteins forming the outer coat of COPII vesicles. In this model, yNup85 and yNup145C form an edge element aligned along the positive curvature of the pore membrane, in analogy to its cousin, the Sec13-Sec31 edge element in COPII. Such arrangement would position the Y-shape with its longer axis almost parallel to the transport axis. In the most recent version of the "lattice" model (26) the Y-shape would be positioned with the stem, central branch point and Nup160 arm following the curvature of the membrane and with the Nup85-Seh1 reaching towards the inside of the pore. Such arrangement predicts that the entire Nup160-Nup37 arm should be positioned closer to the center of the pore than the stalk, with the tip of the arm (Nup160 N-term) approximately at narrowest point of the pore membrane. We observe Nup160 N-term furthest away from the center of the pore, which is inconsistent with this model. **(D)** A head-to-tail model consistent with our observations in two equally plausible versions. For simplicity, we have drawn eight Y-shaped complexes arranged in a ring, however since our data only measures the average radial distance, 16 complexes in a ring would be equally possible. Such an arrangement has been initially suggested by Seo et al. (39) based on the observed interaction between N-terminus of yNup133 and yNup120. The recent EM-tomography study of the human NPC (5) suggested a similar orientation of the Nup107-160, but lacked molecular assignments. A study based on anisotropy of eGFP-Nup133 fusion, showed that Nup133 is oriented with its longer axis perpendicular to the transport axis (24), which is consistent with this arrangement. Apart from providing direct evidence for this arrangement of the Nup107-160 complex, our study clarifies the orientation of the Nup85-Seh1 arm, which had not been addressed previously.
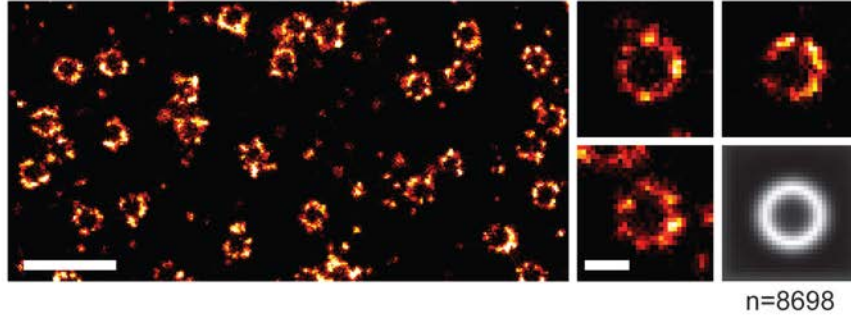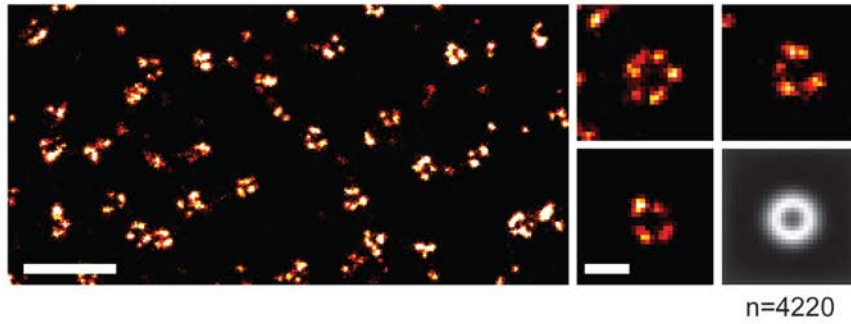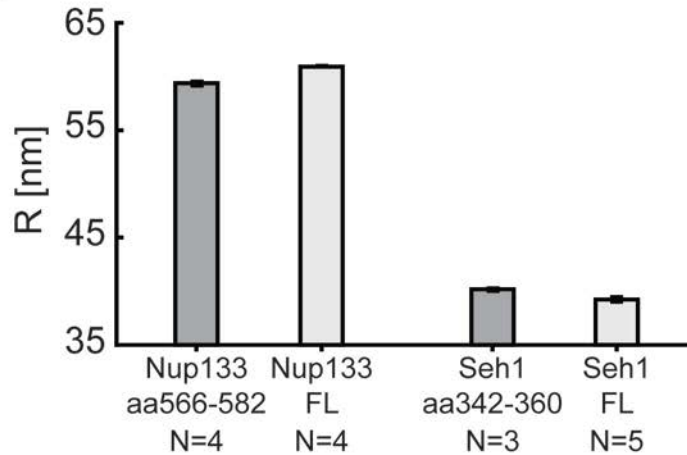
Fig. S6. Validation of positions of immuno-labelled Nup133 and Seh1 with antibodies against full-length proteins.

(**A, B**) Left panels: A representative 4.5 μm^2 area of a lower surface of the nucleus of a U2OS cell stained with Nup133-FL (A) and Seh1-FL (B). Right panels: three exemplary high quality pores and an average image (lower right) generated from n number of aligned particles. Scale bars: 0.5 μm and 0.1 μm from left to right. (**C**) Comparison of average radial positions R of immuno-labels on Nup133 and Seh1 determined using antibodies raised against small peptides (dark gray bars, see Fig. 2) and full-length proteins (light gray bars), measured in N independent experiments. The error bars represent SEM between the experiments. From left to right: Nup133-aa566-582 R = 59.4 ± 0.2 nm, Nup133-FL R = 60.9 ± 0.2 nm, Seh1-aa342-360 R = 40.2 ± 0.1 nm, Seh1-FL R

= 39.2 ± 0.2 nm. The difference between Nup133-aa566-582 and Nup133-FL is significant with a p-value p<0.01; Seh1-aa342-360 and Seh1-FL are not significantly different.
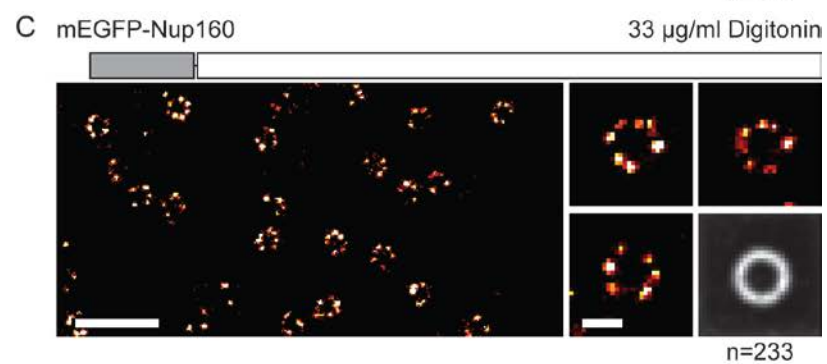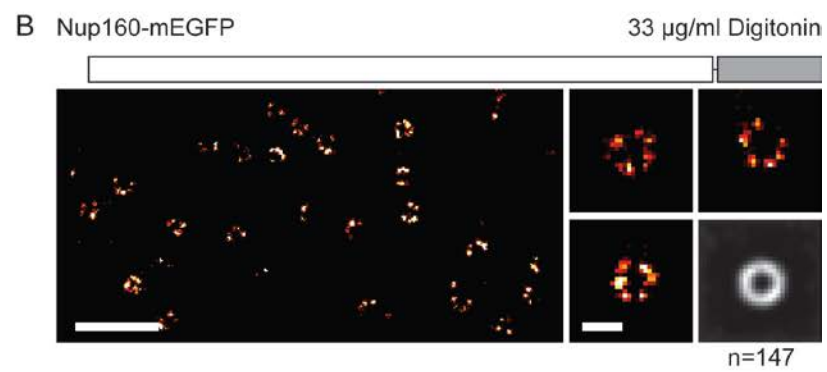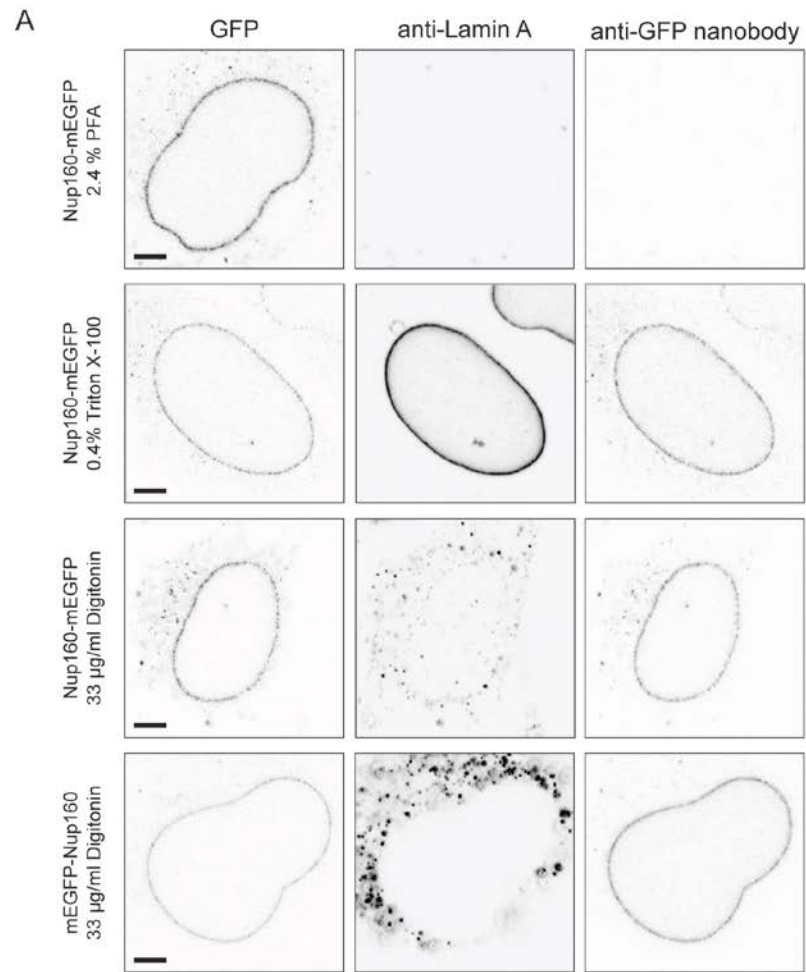
A

| | GFP | anti-Lamin A | anti-GFP nanobody |

Nup160-mEGFP 2.4 % PFA

Nup160-mEGFP 0.4% Triton X-100

Nup160-mEGFP 33 µg/ml Digitonin

mEGFP-Nup160 33 µg/ml Digitonin

B Nup160-mEGFP   33 µg/ml Digitonin

n=147

C mEGFP-Nup160   33 µg/ml Digitonin

n=233

Fig. S7. Nanobodies bind to the Nup160-GFP fusions from the cytoplasm.

(**A**) Confocal images of U2OS cells expressing Nup160-mEGFP or mEGFP-Nup160, stained with 133A2-LaminA antibody and anti-GFP nanobody. The cells were treated with 2.4 % PFA without detergent (first row), 0.4 % Triton and 2.4% PFA (second row) or 33 ug/ml Digitonin and 2.4% PFA (Nup160-mEGFP third row, mEGFP-Nup160 forth row). Scale bar: 5 μm. No nanobody signal was detected in cells treated with PFA only, indicating that the nanobody cannot cross the plasma membrane. The control treatment with Triton that permeabilized both plasma and nuclear membranes showed characteristic Lamin A staining on the rim of the nucleus. In cells treated with Digitonin the plasma membrane was permeabilized while leaving the nuclear envelope intact, as indicated by the absence of Lamin A staining on the rim of the nuclei of these cells. The presence of the nanobody signal indicated that mEGFP is accessible from the cytoplasm. (**B-C**) Left panels: SR images showing a representative 4.5 μm^2 area of a lower surface of the nuclei of a U2OS cells expressing Nup160-C (B) or Nup160-N (C). Right panels: three exemplary high quality pores and an average image (lower right) generated from n number of aligned, quality-controlled pores. Scale bars: 0.5 μm and 0.1 μm from left to right.
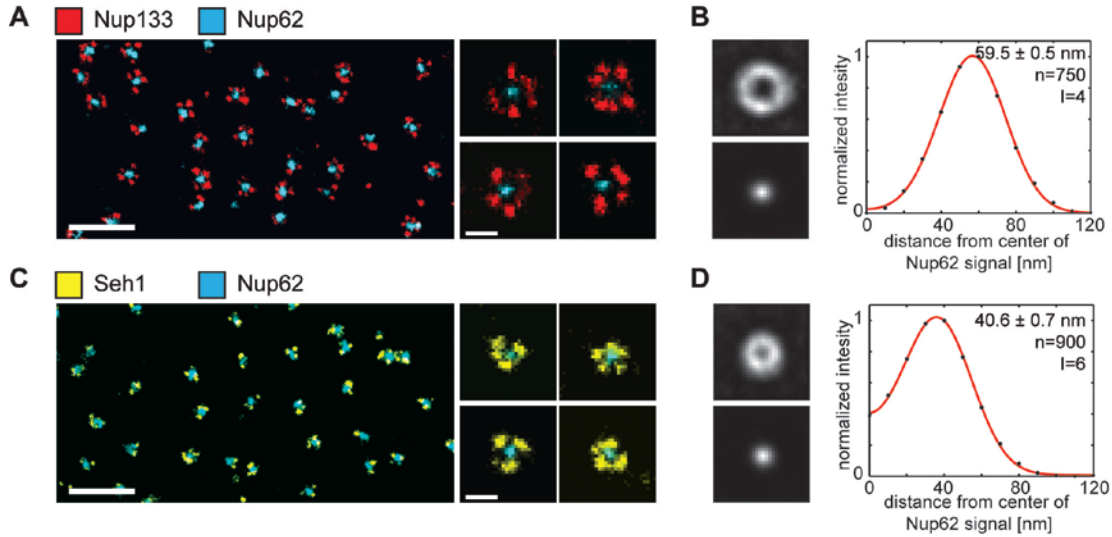
Fig. S8. Particle alignment on a molecular reference.

(A,C) Double color images of pairs of proteins: Nup133 (red) and Nup62 (cyan) (A), Seh1 (yellow) and Nup62 (cyan) (C). Left panels: An image of a representative 4.5 µm² area of the lower surface of the nucleus. Right panels: Four exemplary double stained pores. Scale bars: 0.5 µm and 0.1 µm from left to right. **(B, D)** Left panels: Average images of double-stained pores. The signal from the 642 nm channel (top) was centered on the 532 nm reference (bottom). After alignment, both Nup133 and Seh1 generated the characteristic ring shape. Right panels: Average intensity profiles of 642 nm signal taken around the center of the 532 nm average (black dots), fitted with the circularly convolved Gaussian (Eq. 2) (red line) determined using n number of pores and I number of images. The mean radial distances measured this way show only 0.1 nm (Nup133) and 1.4 nm (Seh1) difference from our single color measurements, (Fig. 2C, H, Fig. S5B, C) demonstrating that alignment on a molecular reference in a second channel can be achieved with high accuracy. The error represents the standard deviation obtained by crossvalidation analysis of five (Nup133-Nup62) and six (Seh1-Nup62) subsets of 150 pores each.
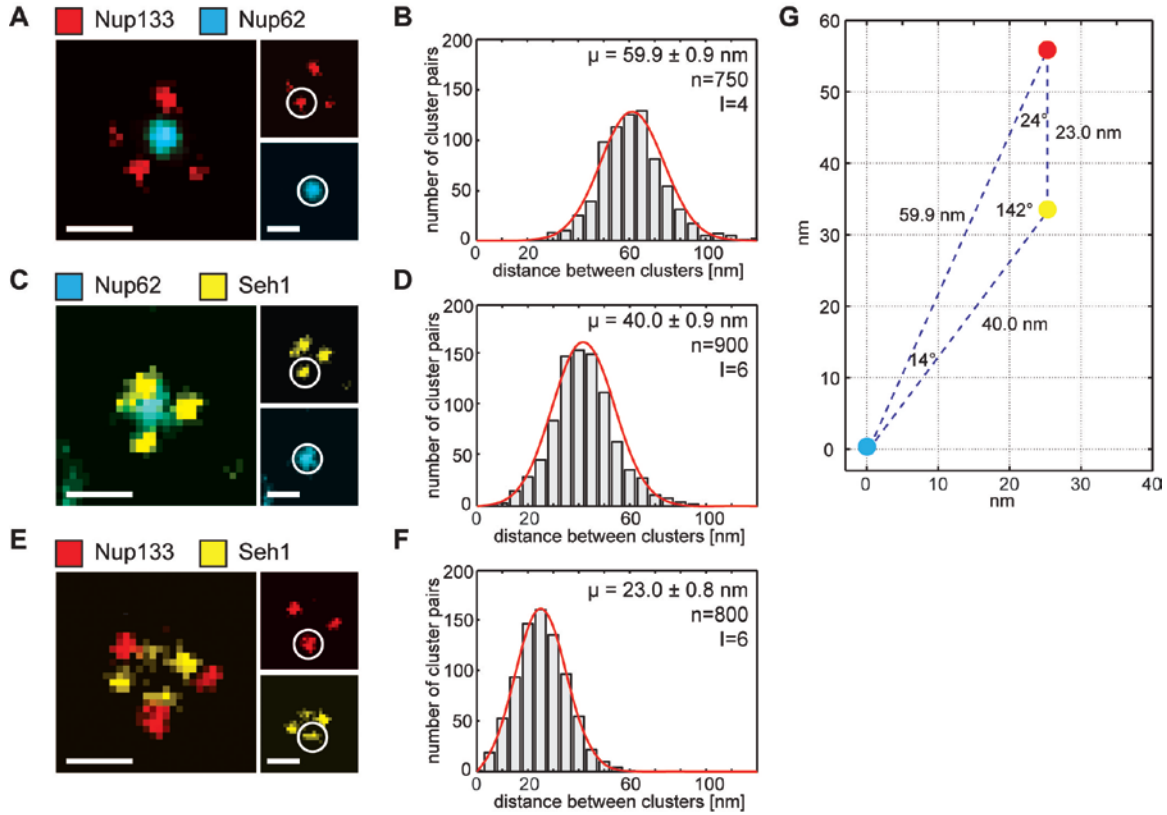
Fig. S9. Relative positions of protein markers can be measured in asymmetric complexes.

Proof-of-principle demonstration of the use of triangulation for mapping of relative positions of three protein markers **(A, C, E)** An artificial dataset was generated using double color images of the following antibody stainings: Nup133 and Nup62 (A), Seh1 and Nup62 (C), Nup133 and Seh1 (E) by manual selection of pairs of localization clusters as indicated in the examples with white circles. Scale bar: 0.1 μm. **(B, D, F)** The distance between n pairs of localization clusters, from I number of images was calculated to generate the distributions presented as histograms. The mean distance μ between the markers was determined from a maximum likelihood fit of the distribution with Eq. 3. The mean distance with the 95% confidence interval is indicated on the histograms. **(G)** Relative positions of the three markers drawn to scale with angles and distances indicated.

Table S1. List of primary antibodies used in this study.

Name	Antigen	Host species	Published in/Supplier
Nup133-FL	full length hsNup133	rabbit	Belgareh et al. (40)
Nup133-aa566-582	amino acids 566-582 of hsNup133	guinea pig	Krull et al. (31)
Nup107-aa33-51	amino acids 33-51 of hsNup107	guinea pig	Hase and Cordes (41)
Nup96-aa880-900	amino acids 880-900 of hsNup96[*]	rabbit	Hase and Cordes (41)
Seh1-FL	full length hsSeh1	rabbit	Platani et al. (42)
Seh1-aa342-360	amino acids 342-360 of hsSeh1	guinea pig	Patre et al. (43)
Nup160-aa941-1436	amino acids 941-1426 of hsNup160	rabbit	Patre et al. (43)
Nup62-aa24-178	amino acids 24-178 of hsNup62	mouse	BD Biosciences
133A2-LaminA	amino acids 598-611 of hsLamin A	mouse	Abcam

*amino acids 1760-1780, Uniprot P52948

Table S2. List of siRNA resistant constructs.

Construct name	CCDS Id[*]	Mutated nucleotides[†]	Tag position	Linker sequence[‡]
pmEGFP-Nup133-s31401res	CCDS1579.1	1170, 1174, 1176	N-term	SGLRSRAQASNSAVD
pEGFP-Nup107-s32727res	CCDS8985.1	1273, 1275, 1278, 1281	N-term	SGLRSRAQASNS
pmEGFP-Nup85-s36612res	CCDS32730.1	972, 975, 978	N-term	SGLRSRAQASNSAVEKAADIT SLYKKVG
pmEGFP-Seh1-s37879res	CCDS45832.1	414, 417, 418	N-term	SGRTQISSSSFEFCSRRYKSGLR S
pmEGFP-Nup160-s23466res	CCDS31484.1	1567, 1569, 1572	N-term	SGLRSRG
pNup160-s23466res-mEGFP	CCDS31484.1	1567, 1569, 1572	C-term	GSGPRDPPVAT
pEGFP-Nup37-s35439res	CCDS9089.1	786-789	N-term	SGLRSRAQASNS

* Consensus CDS database identifier of reference cDNA
† Positions of silent mutations introduced for resistance against indicated siRNA; numbering from the beginning of the CCDS sequence
‡ Amino acid sequence of the linker created between (m)EGFP and Nup
Template cDNA used for generating constructs Nup133, Nup107 and Seh1 constructs was published in Belgareh et al.(40); Nup37 cDNA was published in Cronshaw et al. (27); Nup160 cDNA was a kind gift of Prof. S. Yoshimura; Nup85 cDNA was a generous gift of Dr. Martin Beck.

Table S3. List of siRNAs used in this study.

Gene name	Gene Id[*]	siRNA Id[†]	Sense strand 5' → 3'	Antisense strand 5' → 3'
Nup133	ENSG00000069248	s31401	CUGUAGAAGUCACUC AAUAtt	UAUUGAGUGACUUC UACAGTA
Nup107	ENSG00000111581	s32727	GAUACGAGAGAGCA AUUUAtt	UAAAUUGCUCUCUCG UAUCTA
Nup85	ENSG00000125450	s36612	CCAUUGAUCUGCACU ACUAtt	UAGUAGUGCAGAUC AAUGGGT
Seh1L	ENSG00000085415	s36612	CAGAUGGUAUAGUA AGAAUtt	AUUCUUACUAUACCA UCUGCG
Nup160	ENSG00000030066	s23466	GUUUCGAAAUUUAC AACAAtt	UUGUUGUAAAUUUC GAAACTC
Nup37	ENSG00000075188	s35439	GGUGGUCCACAAUU AGUGAtt	UCACUAAUUGUGGA CCACCTG

[*] ENSEMBL database
[†] Suppliers id

References and Notes

1. R. Reichelt, A. Holzenburg, E. L. Buhle, Jr., M. Jarnik, A. Engel, U. Aebi, Correlation between structure and mass distribution of the nuclear pore complex and of distinct pore complex components. *J. Cell Biol.* **110**, 883–894 (1990). doi:10.1083/jcb.110.4.883 Medline

2. A. Hoelz, E. W. Debler, G. Blobel, The structure of the nuclear pore complex. *Annu. Rev. Biochem.* **80**, 613–643 (2011). doi:10.1146/annurev-biochem-060109-151030 Medline

3. S. G. Brohawn, J. R. Partridge, J. R. R. Whittle, T. U. Schwartz, The nuclear pore complex has entered the atomic age. *Structure* **17**, 1156–1168 (2009). doi:10.1016/j.str.2009.07.014 Medline

4. M. Beck, V. Lucić, F. Förster, W. Baumeister, O. Medalia, Snapshots of nuclear pore complexes in action captured by cryo-electron tomography. *Nature* **449**, 611–615 (2007). doi:10.1038/nature06170 Medline

5. T. Maimon, N. Elad, I. Dahan, O. Medalia, The human nuclear pore complex as revealed by cryo-electron tomography. *Structure* **20**, 998–1006 (2012). doi:10.1016/j.str.2012.03.025 Medline

6. L. Schermelleh, R. Heintzmann, H. Leonhardt, A guide to super-resolution fluorescence microscopy. *J. Cell Biol.* **190**, 165–175 (2010). doi:10.1083/jcb.201002018 Medline

7. M. J. Rust, M. Bates, X. Zhuang, Sub-diffraction-limit imaging by stochastic optical reconstruction microscopy (STORM). *Nat. Methods* **3**, 793–795 (2006). doi:10.1038/nmeth929 Medline

8. J. Fölling, M. Bossi, H. Bock, R. Medda, C. A. Wurm, B. Hein, S. Jakobs, C. Eggeling, S. W. Hell, Fluorescence nanoscopy by ground-state depletion and single-molecule return. *Nat. Methods* **5**, 943–945 (2008). doi:10.1038/nmeth.1257 Medline

9. E. Betzig, G. H. Patterson, R. Sougrat, O. W. Lindwasser, S. Olenych, J. S. Bonifacino, M. W. Davidson, J. Lippincott-Schwartz, H. F. Hess, Imaging intracellular fluorescent proteins at nanometer resolution. *Science* **313**, 1642–1645 (2006). doi:10.1126/science.1127344 Medline

10. S. T. Hess, T. P. K. Girirajan, M. D. Mason, Ultra-high resolution imaging by fluorescence photoactivation localization microscopy. *Biophys. J.* **91**, 4258–4272 (2006). doi:10.1529/biophysj.106.091116 Medline

11. H. Bock, C. Geisler, C. A. Wurm, C. von Middendorff, S. Jakobs, A. Schönle, A. Egner, S. W. Hell, C. Eggeling, Two-color far-field fluorescence nanoscopy based on photoswitchable emitters. *Appl. Phys. B* **88**, 161–165 (2007). doi:10.1007/s00340-007-2729-0

12. M. Heilemann, S. van de Linde, M. Schüttpelz, R. Kasper, B. Seefeldt, A. Mukherjee, P. Tinnefeld, M. Sauer, Subdiffraction-resolution fluorescence imaging with

conventional fluorescent probes. *Angew. Chem. Int. Ed.* **47**, 6172–6176 (2008). doi:10.1002/anie.200802376 Medline

13. A. Löschberger, S. van de Linde, M. C. Dabauvalle, B. Rieger, M. Heilemann, G. Krohne, M. Sauer, Super-resolution imaging visualizes the eightfold symmetry of gp210 proteins around the nuclear pore complex and resolves the central channel with nanometer resolution. *J. Cell Sci.* **125**, 570–575 (2012). [doi:10.1242/jcs.098822](doi:10.1242/jcs.098822) Medline

14. For details see Supplemental Material.

15. M. Lutzmann, R. Kunze, A. Buerer, U. Aebi, E. Hurt, Modular self-assembly of a Y-shaped multiprotein complex from seven nucleoporins. *EMBO J.* **21**, 387–397 (2002). doi:10.1093/emboj/21.3.387 Medline

16. M. Kampmann, G. Blobel, Three-dimensional structure and flexibility of a membrane-coating module of the nuclear pore complex. *Nat. Struct. Mol. Biol.* **16**, 782–788 (2009). doi:10.1038/nsmb.1618 Medline

17. S. Bilokapic, T. U. Schwartz, 3D ultrastructure of the nuclear pore complex. *Curr. Opin. Cell Biol.* **24**, 86–91 (2012). [doi:10.1016/j.ceb.2011.12.011](doi:10.1016/j.ceb.2011.12.011) Medline

18. S. G. Brohawn, N. C. Leksa, E. D. Spear, K. R. Rajashankar, T. U. Schwartz, Structural evidence for common ancestry of the nuclear pore complex and vesicle coats. *Science* **322**, 1369–1373 (2008). doi:10.1126/science.1165886 Medline

19. K.-C. Hsia, P. Stavropoulos, G. Blobel, A. Hoelz, Architecture of a coat for the nuclear pore membrane. *Cell* **131**, 1313–1326 (2007). doi:10.1016/j.cell.2007.11.038 Medline

20. F. Alber, S. Dokudovskaya, L. M. Veenhoff, W. Zhang, J. Kipper, D. Devos, A. Suprapto, O. Karni-Schmidt, R. Williams, B. T. Chait, A. Sali, M. P. Rout, The molecular architecture of the nuclear pore complex. *Nature* **450**, 695–701 (2007). doi:10.1038/nature06405 Medline

21. J. Ries, C. Kaplan, E. Platonova, H. Eghlidi, H. Ewers, A simple, versatile method for GFP-based super-resolution microscopy via nanobodies. *Nat. Methods* **9**, 582–584 (2012). doi:10.1038/nmeth.1991 Medline

22. M. P. Rout, J. D. Aitchison, A. Suprapto, K. Hjertaas, Y. Zhao, B. T. Chait, The yeast nuclear pore complex: composition, architecture, and transport mechanism. *J. Cell Biol.* **148**, 635–651 (2000). [doi:10.1083/jcb.148.4.635](doi:10.1083/jcb.148.4.635) Medline

23. J. Fernandez-Martinez, J. Phillips, M. D. Sekedat, R. Diaz-Avalos, J. Velazquez-Muriel, J. D. Franke, R. Williams, D. L. Stokes, B. T. Chait, A. Sali, M. P. Rout, Structure-function mapping of a heptameric module in the nuclear pore complex. *J. Cell Biol.* **196**, 419–434 (2012). [doi:10.1083/jcb.201109008](doi:10.1083/jcb.201109008) Medline

24. M. Kampmann, C. E. Atkinson, A. L. Mattheyses, S. M. Simon, Mapping the orientation of nuclear pore proteins in living cells with polarized fluorescence microscopy. *Nat. Struct. Mol. Biol.* **18**, 643–649 (2011). doi:10.1038/nsmb.2056 Medline

25. E. W. Debler, Y. Ma, H. S. Seo, K. C. Hsia, T. R. Noriega, G. Blobel, A. Hoelz, A fence-like coat for the nuclear pore membrane. *Mol. Cell* **32**, 815–826 (2008). doi:10.1016/j.molcel.2008.12.001 Medline

26. S. Bilokapic, T. U. Schwartz, Molecular basis for Nup37 and ELY5/ELYS recruitment to the nuclear pore complex. *Proc. Natl. Acad. Sci. U.S.A.* **109**, 15241–15246 (2012). doi:10.1073/pnas.1205151109 Medline

27. J. M. Cronshaw, A. N. Krutchinsky, W. Zhang, B. T. Chait, M. J. Matunis, Proteomic analysis of the mammalian nuclear pore complex. *J. Cell Biol.* **158**, 915–927 (2002). doi:10.1083/jcb.200206106 Medline

28. A. Ori, N. Banterle, M. Iskar, A. Andrés-Pons, C. Escher, H. Khanh Bui, L. Sparks, V. Solis-Mezarino, O. Rinner, P. Bork, E. A. Lemke, M. Beck, Cell type-specific nuclear pores: a case in point for context-dependent stoichiometry of molecular machines. *Mol. Syst. Biol.* **9**, 648 (2013). doi:10.1038/msb.2013.4 Medline

29. E. L. Snapp, R. S. Hegde, M. Francolini, F. Lombardo, S. Colombo, E. Pedrazzini, N. Borgese, J. Lippincott-Schwartz, Formation of stacked ER cisternae by low affinity protein interactions. *J. Cell Biol.* **163**, 257–269 (2003). doi:10.1083/jcb.200306020 Medline

30. H. Erfle, B. Neumann, P. Rogers, J. Bulkescher, J. Ellenberg, R. Pepperkok, Work flow for multiplexing siRNA assays by solid-phase reverse transfection in multiwell plates. *J. Biomol. Screen.* **13**, 575–580 (2008). doi:10.1177/1087057108320133 Medline

31. S. Krull, J. Dörries, B. Boysen, S. Reidenbach, L. Magnius, H. Norder, J. Thyberg, V. C. Cordes, Protein Tpr is required for establishing nuclear pore-associated zones of heterochromatin exclusion. *EMBO J.* **29**, 1659–1673 (2010). doi:10.1038/emboj.2010.54 Medline

32. M. Bates, G. T. Dempsey, K. H. Chen, X. Zhuang, Multicolor super-resolution fluorescence imaging via multi-parameter fluorophore detection. *ChemPhysChem* **13**, 99–107 (2012). doi:10.1002/cphc.201100735 Medline

33. B. Huang, W. Wang, M. Bates, X. Zhuang, Three-dimensional super-resolution imaging by stochastic optical reconstruction microscopy. *Science* **319**, 810–813 (2008). doi:10.1126/science.1153529 Medline

34. C. D. Kuglin, D. C. Hines, The phase correlation image alignment method, in *Proc. IEEE 1975 Inf. Conf Cybernet. Society* (1975), pp. 163–16.

35. Prof. Thomas C. O'Have, Matlab File Exchange.

36. Y. Benjamini, Y. Hochberg, Controlling the false discovery rate: a practical and powerful approach to multiple testing. *J. R. Stat. Soc., B* **57**, 289–300 (1995).

37. R. Hermann, P. Walther, M. Müller, Immunogold labeling in scanning electron microscopy. *Histochem. Cell Biol.* **106**, 31–39 (1996). doi:10.1007/BF02473200 Medline

38. L. S. Churchman, H. Flyvbjerg, J. A. Spudich, A non-Gaussian distribution quantifies distances measured with fluorescence localization techniques. *Biophys. J.* **90**, 668–671 (2006). doi:10.1529/biophysj.105.065599 Medline

39. H.-S. Seo, Y. Ma, E. W. Debler, D. Wacker, S. Kutik, G. Blobel, A. Hoelz, Structural and functional analysis of Nup120 suggests ring formation of the Nup84 complex. *Proc. Natl. Acad. Sci. U.S.A.* **106**, 14281–14286 (2009). doi:10.1073/pnas.0907453106 Medline

40. N. Belgareh, G. Rabut, S. W. Baï, M. van Overbeek, J. Beaudouin, N. Daigle, O. V. Zatsepina, F. Pasteau, V. Labas, M. Fromont-Racine, J. Ellenberg, V. Doye, An evolutionarily conserved NPC subcomplex, which redistributes in part to kinetochores in mammalian cells. *J. Cell Biol.* **154**, 1147–1160 (2001). [doi:10.1083/jcb.200101081](doi:10.1083/jcb.200101081) Medline

41. M. E. Hase, V. C. Cordes, Direct interaction with nup153 mediates binding of Tpr to the periphery of the nuclear pore complex. *Mol. Biol. Cell* **14**, 1923–1940 (2003). [doi:10.1091/mbc.E02-09-0620](doi:10.1091/mbc.E02-09-0620) Medline

42. M. Platani, R. Santarella-Mellwig, M. Posch, R. Walczak, J. R. Swedlow, I. W. Mattaj, The Nup107-160 nucleoporin complex promotes mitotic events via control of the localization state of the chromosome passenger complex. *Mol. Biol. Cell* **20**, 5260–5275 (2009). [doi:10.1091/mbc.E09-05-0377](doi:10.1091/mbc.E09-05-0377) Medline

43. M. Patre, A. Tabbert, D. Hermann, H. Walczak, H. R. Rackwitz, V. C. Cordes, E. Ferrando-May, Caspases target only two architectural components within the core structure of the nuclear pore complex. *J. Biol. Chem.* **281**, 1296–1304 (2006). [doi:10.1074/jbc.M511717200](doi:10.1074/jbc.M511717200) Medline